GEOPHYSICS, VOL. 89, NO. 5 (SEPTEMBER-OCTOBER 2024); P. G93–G108, 22 FIGS., 4 TABLES.
10.1190/GEO2023-0551.1

Recovering 3D salt dome by gravity data inversion using ResU-Net++

Minghao Xian[1], Zhengwei Xu[1], Michael S. Zhdanov[2], Yaming Ding[3], Rui Wang[3], Xuben Wang[1], Jun Li[1], and Guangdong Zhao[1]

ABSTRACT

In geophysical research, gravity-based inversion is essential for identifying geologic anomalies, mapping rock structures, and extracting resources such as oil and minerals. However, traditional gravity inversion methods face challenges, such as the volumetric effects of gravity fields and the management of large complex matrices. Unsupervised learning techniques often struggle with overfitting and interpreting gravity data. This study explores the application of various U-Net-based network architectures in gravity inversion, each offering distinct challenges and advantages. Nested U-Net, although effective, requires a high parameter count, leading to extended training periods. The recurrent residual U-Net's implicit attention mechanism restricts its dynamic adaptability, whereas the attention U-Net's lack of residual connections raises concerns about gradient issues. This research comprehensively analyzes the training processes, core functionalities, and module distribution of these networks, including the residual U-Net++. Our synthetic studies compare these networks with traditional focused regularized gravity inversion for reconstructing density anomalies. The results demonstrate that the nested U-Net closely approximates the actual model despite some redundancy. The recurrent residual U-Net indicates an improved alignment with minimal redundancies, and the attention U-Net is effective in density prediction but encounters difficulties in areas of low density. Notably, the residual U-Net++ excels in inversion modeling, achieving the lowest misfit percentage and accurately replicating density values. In practical applications, the residual U-Net++ impressively reconstructs the F2 salt diapir in the Nordkapp Basin with well-defined boundaries that closely match seismic data interpretations. These results underscore the capabilities of the residual U-Net++ in geophysical data analysis, structural reconstruction, and inversion, demonstrating its effectiveness in simulated settings and real-world scenarios.

INTRODUCTION

Gravity-based exploration plays a pivotal role in geophysical investigations, significantly impacting the identification of geologic anomalies, the delineation of rock structures, and the management of engineering geologic surveys. It also serves as an essential tool in exploring oil, gas, and mineral resources (Cai and Zhdanov, 2015; Layade et al., 2020; Alaofin, 2022; Li et al., 2023; Sampietro et al., 2023).

In a geophysical context, gravity inversion is often an ill-posed problem (Zhdanov, 2015; Xu et al., 2021a, 2021b; Liang et al., 2023). The root of this challenge stems from the disparity between the volume of observed data and the magnitude of potential solutions; even minor fluctuations in the data can dramatically alter the solution, making it nonunique and unstable. Therefore, selecting an appropriate inversion method is crucial for addressing the issue of solution multiplicity.

Conventional gravity inversion can be categorized into deterministic inversion (Marquardt, 1963; Backus and Gilbert, 1967; Backus and Gilbert, 1968; Backus, 1970a, 1970b; Tikhonov and Arsenin, 1977; Wei and Sun, 2021) and probabilistic inversion (Foster, 1961; Franklin, 1970; Jackson, 1972; Tarantola and Valette, 1982; Tarantola, 2005; Wei and Sun, 2022). The former encompasses methods such as Newton's approach (Zhang et al., 2021), the

Manuscript received by the Editor 23 September 2023; revised manuscript received 3 May 2024; published ahead of production 23 May 2024; published online 5 August 2024.
[1]Chengdu University of Technology, Key Laboratory of Earth Exploration and Information Techniques of Ministry of Education, Chengdu, China and Chengdu University of Technology, College of Geophysics, Chengdu, China. E-mail: xmhcdut@163.com; zhengwei.xu@cdut.edu.cn (corresponding author); wxb@cdut.edu.cn; lijun3@cdut.edu.cn; guangdongzhao@cdut.edu.cn.
[2]University of Utah, Department of Geology & Geophysics, Salt Lake City, Utah, USA; TechnoImaging, LLC, Salt Lake City, Utah, USA; and Moscow Institute of Physics and Technology (MFTI), Zhukovsky, Russia. E-mail: michael.s.zhdanov@gmail.com.
[3]Changchun University of Science and Technology, Changchun, China. E-mail: dingyaming@mails.cust.edu.cn; wangrui56789@163.com.
© 2024 Society of Exploration Geophysicists. All rights reserved.

Downloaded from http://pubs.geoscienceworld.org/seg/geophysics/article-pdf/89/5/G93/6947062/geo-2023-0551.1.pdf
by Univ Utah Marriott Library user

steepest descent method (Tseng and Lee, 2021), and the conjugate gradient method (Qin et al., 2016; Gao and Huang, 2017; Wang et al., 2017; Tian et al., 2019). However, these gradient minimization techniques often struggle to escape from deep local minima, particularly when error functions exhibit multiple local minima.

The Monte Carlo method provides a partial remedy by reducing the likelihood of the gradient method becoming ensnared in local minima (Press, 1968, 1970a, 1970b; Sambridge and Mosegaard, 2002; Wei et al., 2023). This method is divided into two main approaches. The first involves an exhaustive random search that aims to resolve model parameters by generating predictive data that closely approximate the observed data, thus identifying the global minimum of the error function. Although effective, this method can be susceptible to entrapment in multiple local minima (Keilis-Borok and Yanovskaja, 1967) and may necessitate numerous steps for a thorough search. To mitigate this, the second approach incorporates optimization algorithms to streamline the search process, with techniques such as simulated annealing (Nagihara and Hall, 2001) — inspired by metallurgical heating and cooling processes — and the genetic algorithm (Montesinos et al., 2005), which mimics natural evolutionary processes. Despite these innovations, traditional gravity inversion still faces challenges in addressing the volumetric effects of gravity fields, matrix underdetermination, and management of large ill-conditioned matrices.

The advent of machine-learning (ML) methods that incorporate a priori geologic information to resolve inverse problems has been garnering considerable interest. Numerous studies have explored the application of unsupervised ML algorithms, guided by prior geologic insights, to address the challenges in gravity inversion. Key techniques include clustering (Liu and Jin, 2020), linear classifiers (Marques-Silva et al., 2020), support vector machines (Li et al., 2020), decision trees (Özbeyaz and Söylemez, 2020), and stochastic prediction (Amiramjadi et al., 2023). These methods have been used to mitigate the inherent ill-posedness of geophysical inverse problems. In addition, methods such as linear regression (Leggetter and Woodland, 1995), logistic regression (Paul, 2009), and polynomial regression (Ruppert, 1997) have proven effective in revealing subsurface physical properties. However, a major challenge remains in establishing clear objectives or benchmarks to evaluate the performance of these algorithms. Determining whether identified patterns or structures are meaningful or merely coincidental remains complex. Furthermore, unsupervised learning is prone to overfitting and presents difficulties in result interpretation.

In the realm of ML, supervised learning demonstrates superior generalization capabilities over unsupervised learning, owing to its reliance on labeled data during the training process. This reliance allows for easier performance evaluation and adjustments during the algorithm's learning phase (Wu et al., 2023). Deep learning, a subset of supervised learning, primarily focuses on training multilayer neural networks to extract hierarchical representations from complex data. Initially, the backpropagation neural network was foundational in deep learning's application to gravity exploration (Guan et al., 1998; Chen et al., 2018; Sun et al., 2022; Delcey et al., 2023; Wang et al., 2023). However, limitations such as parameter scalability and generalization capacity prompted geophysicists to adopt convolutional neural networks (CNNs). Known for their local connections and shared weights, CNNs offer enhanced generalization and transfer learning capabilities, crucial for effectively extracting and modeling geophysical field characteristics (Zhao et al., 2020; He et al., 2021; Annan and Wan, 2022). Nonetheless, to capture detailed subsurface structures and precise boundary information, it is crucial to maintain extensive local and location data. Traditional CNNs, focusing primarily on global information, often fall short in predicting complex geologic phenomena accurately.

The U-Net architecture, integrating encoder and decoder mechanisms, excels in semantic information extraction and spatial detail restoration in image segmentation tasks (Ronneberger et al., 2015; Jiang et al., 2021; Chen et al., 2023; Liu et al., 2023; Wang et al., 2024). Despite its strengths, U-Net faces challenges in handling the inversion of intricate geologic structures due to its uniform weighting of features at equivalent levels during the encoding and decoding processes, which can obscure critical geologic features under less significant ones.

Recent innovations have led to the development of U-Net derivatives, enhancing performance and generalization in image segmentation. Notably, the nested U-Net, proposed by Zhou et al. (2018), features a deeply nested structure that integrates multilevel features, enabling simultaneous processing of feature information across different scales. This architecture enhances the understanding of local and global geologic contexts and reduces information loss, proving effective in reconstructing subsurface structures (Zhang and Sheng, 2020; Gao et al., 2021). However, due to its deep and complex architecture, its complexity requires significant computational resources and training time.

The recurrent residual U-Net (R2U-Net), introduced by Alom et al. (2018), mitigates the high parameter count of traditional networks by incorporating recurrent residual units (R2Us), simplifying the network and reducing overfitting risks. Nevertheless, its implicit attention mechanism limits dynamic feature weighting adjustment, curbing its application in diverse geophysical surveys. In contrast, the attention U-Net (AttU-Net), introduced by Oktay et al. (2018), uses an explicit attention mechanism that dynamically adjusts feature weights, significantly enhancing generalization for geophysical applications (Tian et al., 2022; Sui et al., 2023). However, the absence of residual connections in AttU-Net raises concerns about potential gradient vanishing issues.

Recently, the residual U-Net++ (ResU-Net++) network, proposed by Jha et al. (2019), incorporates residual connections, which facilitate more direct gradient propagation, effectively addressing the issue of gradient vanishing. In addition, the integration of the squeeze-and-excitation (S-E) module, a lightweight attention mechanism, significantly enhances the network's ability to discern local and global geophysical features. Furthermore, the atrous-spatial-pyramid-pooling (ASPP) module of ResU-Net++ captures semantic information at various scales, improving the accuracy and robustness of the segmentation efforts. Despite these technological advances, ResU-Net++ has not been widely adopted in geophysical applications yet. The limited application of these four network types in geophysical inversion has resulted in scarce research on their ability to accurately and efficiently reconstruct underground geologic structures, particularly considering their unique structural differences.

This study details the training methodologies, operational principles, and core functionalities of four U-Net-based networks: the nested U-Net, R2U-Net, AttU-Net, and ResU-Net++. We compare the distribution of their main feature modules and systematically evaluate their performance against traditional focused regularized

Downloaded from http://pubs.geoscienceworld.org/seg/geophysics/article-pdf/89/5/G93/6947062/geo-2023-0551.1.pdf
by Univ Utah Marriott Library user

inversion in density imaging tasks. The validation process is segmented into two primary phases to assess the networks' effectiveness in synthetic environments and real-world applications. Initially, we generate extensive data sets for the simulation, train the networks, and establish the verification models to compare each network's effectiveness against conventional inversion methods. In the second phase, the network showing the most promising results from the simulation tests is selected to perform an inversion on actual gravity data from the salt dome geologic structures in the Nordkapp Basin.

INVERSION METHODOLOGY BASED ON U-NET NETWORKS

Generation of training sets

Achieving precision in the attributes of density, depth, and size of geologic targets necessitates the development of a detailed training sample set that encompasses a diverse array of geologic body shapes. This set should ideally mirror the most likely distributions of the geologic bodies and their corresponding gravity anomalies. Thus, selecting appropriate techniques and parameters to construct a training set that offers optimal performance, wide applicability, and the ability to mimic real-world data distribution presents a significant challenge.

For gravity data forward modeling, we initially divided the lower half-space of the observation area (4000 m × 4000 m × 4000 m) into 20 × 20 × 20 rectangular prisms, each measuring 200 m on each side (Figure 1). In constructing the model, we uniformly assigned a density of 1 g/cm^3 to each prism. To mitigate the boundary effects, we excluded at least three cells (cumulatively 600 m) along the model's perimeter.

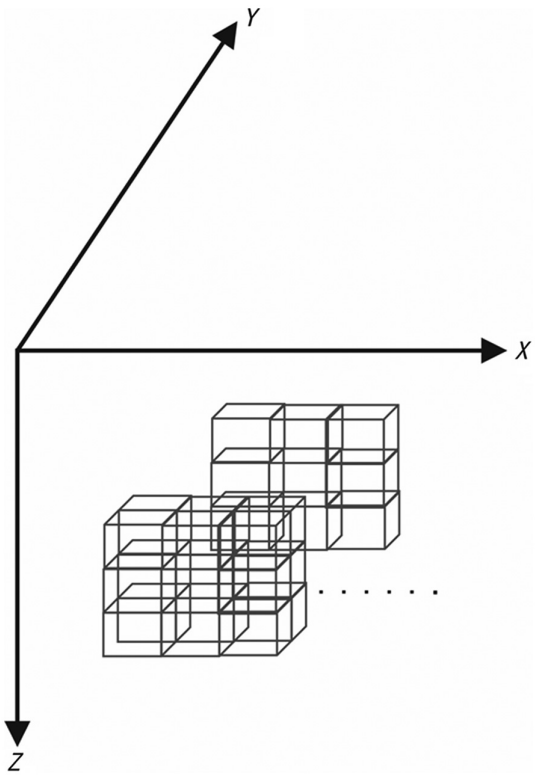

Figure 1. Schematic illustration of the lower half-space in the observation area partitioned into 20 × 20 × 20 rectangular prisms for the application of gravity data forward modeling. Each prism measures 200 m × 200 m × 200 m.

To simulate a wide variety of geologic bodies that exhibit gravity anomalies, we used two distinct model generation methods. The first method creates "separated combined models" from two independently generated simple models. The second method, "contact assembly models," integrates multiple individual models under specific constraints, differing from the separated models that stem from randomly selected single models within predefined constraints. Figure 2 shows four randomly chosen data sets, each varying in size and shape, to demonstrate this methodology. Overall, we produced a total of 10,000 model sets, allocating 8000 for neural network training and 2000 for validation purposes.

Following this, the corresponding gravity responses, denoted as $\{\mathbf{g}_z^{\psi}\}_{\psi=1}^{N}, N = 10{,}000$, are simulated using forward modeling. The vertical component of the gravity field, denoted as $g_z(\mathbf{r})$, can be mathematically represented by the equation $g_z(\mathbf{r}) = \mathbf{A}_z(\rho) = \gamma \iiint_D (\rho(\mathbf{r}')/|\mathbf{r}' - \mathbf{r}|^3) K_z(\mathbf{r}' - \mathbf{r}) dv'$, where $r \notin D$. Here, γ symbolizes the gravitational constant ($\gamma = 6.67384 \times 10^{-11}$ m^3/kg · s^2), ρ represents the density distribution within some anomalous domain D in the subsurface, and $\mathbf{A}_z$ represents the corresponding linear operators of forward modeling. The kernels $K_z(\mathbf{r}' - \mathbf{r}) = z' - z$. This formulation is essential for calculating the gravitational influence of a specified density distribution on the surrounding points in space, typically used in gravity inversion tasks to model subsurface structures.

From these simulations, interior features are extracted to establish their inherent relationship with the labeled information. Figure 3b shows the forward-modeled vertical component of the gravitational data g_z computed from the density model (Figure 3a).

Overview of the structures of the U-Net-based networks

Nested U-Net network

The nested U-Net network represents a significant advancement in deep-learning architectures for geophysical applications. It incorporates a nested structure within the traditional U-Net framework, which allows it to capture multiscale gravity-density features at

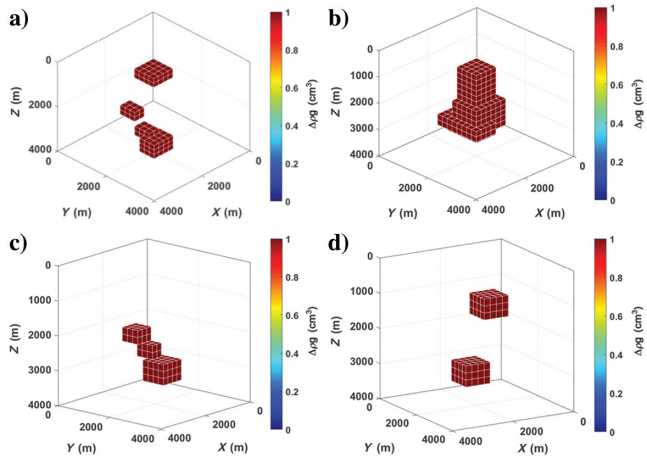

Figure 2. Four arbitrarily selected data sets: (a and d) the separated combined model and (b and c) the contact assembly model.

Downloaded from http://pubs.geoscienceworld.org/seg/geophysics/article-pdf/89/5/G93/6947062/geo-2023-0551.1.pdf
by Univ Utah Marriott Library user

various depths. This innovative approach improves segmentation accuracy and robustness, while effectively mitigating gradient vanishing issues and optimizing parameter sharing and memory usage for more stable and efficient training.

The architecture is shown in Figure 4a. The encoder, outlined in a dotted gray box, alternates between convolutional layers for feature extraction and downsampling (pooling) layers to reduce spatial dimensions while preserving important features. This is followed by a U-shaped connection module that links feature maps from different encoder levels to corresponding levels in the decoder, enhancing the flow of information.

Figure 4b details the nested architecture. During the encoding phase, the convolutional layers (denoted as $X^{i,j}$) extract and process local information through filters, achieving a detailed representation of the gravity field image. The downsampling layers aim to condense the feature map's spatial dimensions, using maximum pooling to maintain crucial features. The integrated U-shaped configuration between the encoder and decoder maintains multiscale feature information, minimizing information loss and resolution degradation, which is crucial for precise target localization and segmentation. In the decoding phase, the upsampling layers gradually restore and enlarge the feature map from the encoder to match the size of the original input image. Concurrently, the convolutional layers further refine and enhance these features, improving the semantic richness of the output, which is critical for accurate image segmentation and gravity field interpretation.

Diverging from traditional network formulas, the mathematical expression for the nested structure is unique. As shown in Figure 4c, $X^{i,j}$ represents different nodes. The relationship between $X^{0,0}$ and $X^{0,1}$ is defined as $X^{0,1} = H[X^{0,0}, U(X^{1,0})]$, where H is the convolution operation followed by the activation function, U signifies the upsampling layer, and $[\cdots]$ indicates the cascading layer. From this recursion, we derive $X^{0,4} = H[X^{0,0}, X^{0,1}, X^{0,2}, X^{0,3}, U(X^{1,2})]$, showcasing the intricate relationship between various layers and their functions within the network.

R2U-Net network

The R2U-Net network stands out in the landscape of deep-learning architectures, distinguished by its innovative R2U structure. This design ingeniously merges the functionalities of recurrent and residual connections, significantly enhancing the efficiency of feature extraction and information transfer. R2U-Net is adept at capturing local and global features within images, improving segmentation accuracy and robustness. Its streamlined parameter count and reduced computational complexity make it exceptionally effective in environments with limited resources.

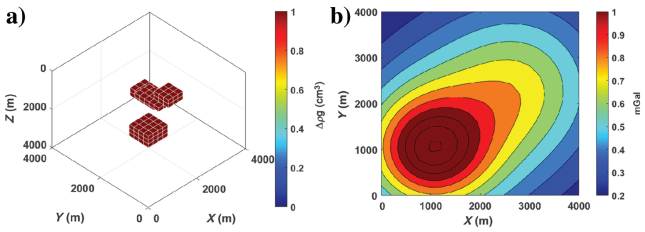

Figure 3. (a) Randomly selected density model and (b) forward-modeled gravity data.

Figure 5a shows the structural design of R2U-Net, in which the core features the integration of the recurrent neural networks, which bolsters the network's capability of representing features and transmitting contextual information through recurrent connections. In its encoder phase, R2U-Net adopts a layout similar to U-Net, consisting of convolutional and pooling layers, wherein the convolutional layer is tasked with extracting diverse feature information from the gravity image, using various filters to process local and global information, thereby encoding image features. The pooling layers focus on reducing the feature map size while preserving critical data and minimizing the number of parameters, thereby facilitating the multiscale feature extraction and encoding into a comprehensive 3D density representation. The decoder phase mirrors this structure, comprised of upsampling layers and convolutional modules, where the upsampling layer methodically restores and enlarges the feature map from the encoder, aligning its dimensions with those of the

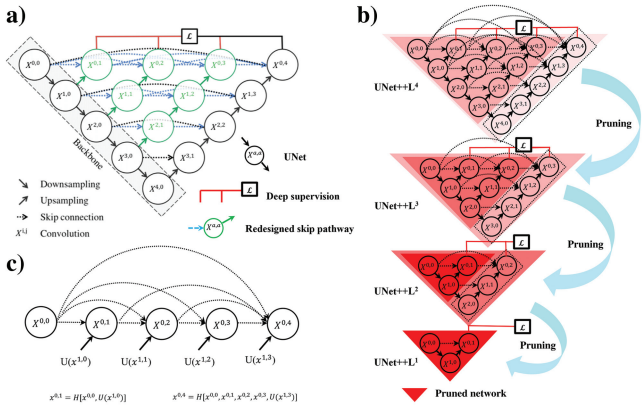

Figure 4. Overview of the structures of the nested U-net network: (a) structural design with an encoder and decoder, (b) structure diagram of the nested architecture, and (c) detailed schematic diagram of the nested architecture (modified from Zhou et al., 2018).

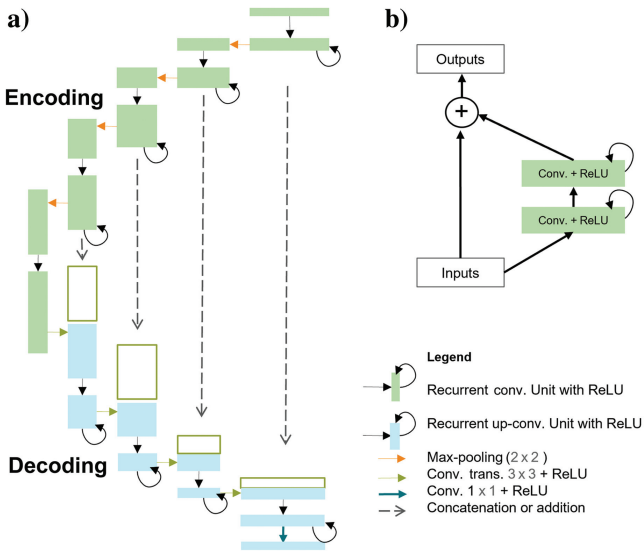

Figure 5. Overview of the structures of the R2U-Net network: (a) structure diagram of the nested architecture and (b) schematic diagram of R2U (modified from Alom et al., 2018).

Downloaded from http://pubs.geoscienceworld.org/seg/geophysics/article-pdf/89/5/G93/6947062/geo-2023-0551.1.pdf
by Univ Utah Marriott Library user

original input image. The convolutional layer furthers this process by extracting and refining features for a more semantically rich feature representation.

Figure 5b shows each R2U, which consist of two sequential convolution blocks. Each block includes a rectified linear unit (ReLU) layer, a 3×3 convolution layer, and residual connections, which are crucial for capturing long-term dependencies and contextual information. This enhances the network's semantic understanding and generalization ability, especially in the domain of geophysical gravity inversion. Here, R2U-Net's residual structures play a vital role in training deep neural networks to manage gravity-related data, countering the increased training errors and issues such as "gradient dispersion or explosion" common with deeper networks. The incorporation of residual units not only simplifies the training process but also ensures the seamless flow of gravity information through the network. Consequently, R2U-Net exhibits superior performance, surpassing traditional deep-learning models in the precision and accuracy of geophysical model predictions.

AttU-Net network

The AttU-Net network is at the forefront of deep-learning innovations, notably distinguished by its integration of an attention gate (AG) module. This module significantly enhances the network's capacity to pinpoint and process key features at local and global scales, thereby boosting the efficiency of feature extraction and information transfer. These enhancements lead to increased accuracy and robustness in segmentation tasks, making AttU-Net particularly effective in resource-constrained settings due to its low parameter count and reduced computational complexity.

As shown in Figure 6a, the structure of the AttU-Net in the encoder phase follows the U-Net design, featuring convolutional and pooling layers enriched with an AG module. The decoder consists of alternating upsampling and convolutional layers. Similar to R2U-Net, the AttU-Net's encoder uses convolution layers to extract and encode detailed feature information, whereas the pooling layers refine the feature maps, strategically preserving essential features for advanced semantic segmentation. The decoder's layers play a pivotal role in meticulously reconstructing the image's detailed and semantic aspects, which is crucial for precise pixel-level classification and segmentation.

The AG module, as shown in Figure 6b, is vital for dynamically adjusting the weights of the feature map, enabling focused enhancement of the features critical for segmentation tasks. This module increases the network's sensitivity and capacity to identify and emphasize essential features by merging the feature map from the encoder with attentively adjusted weights. The selective enhancement of relevant gravity information by the AG module ensures that the network prioritizes crucial data over less significant details, effectively filtering out irrelevant data. This targeted approach not only streamlines the feature mapping process but also significantly improves the efficiency and accuracy of gravity inversion tasks. Detailed information about the AG module is given in Appendix A.

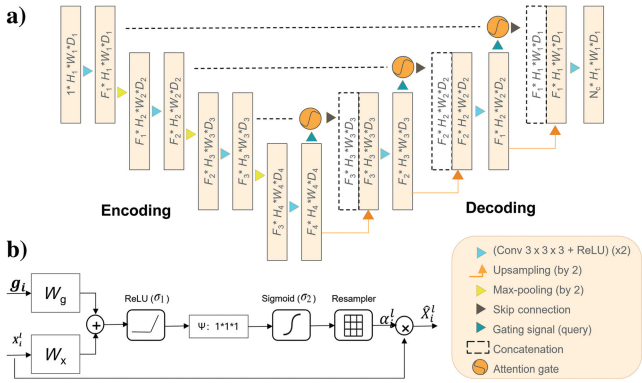

Figure 6. Overview of the structures of the AttU-Net network: (a) structural diagram and (b) structure diagram of the AG module (modified from Oktay et al., 2018).

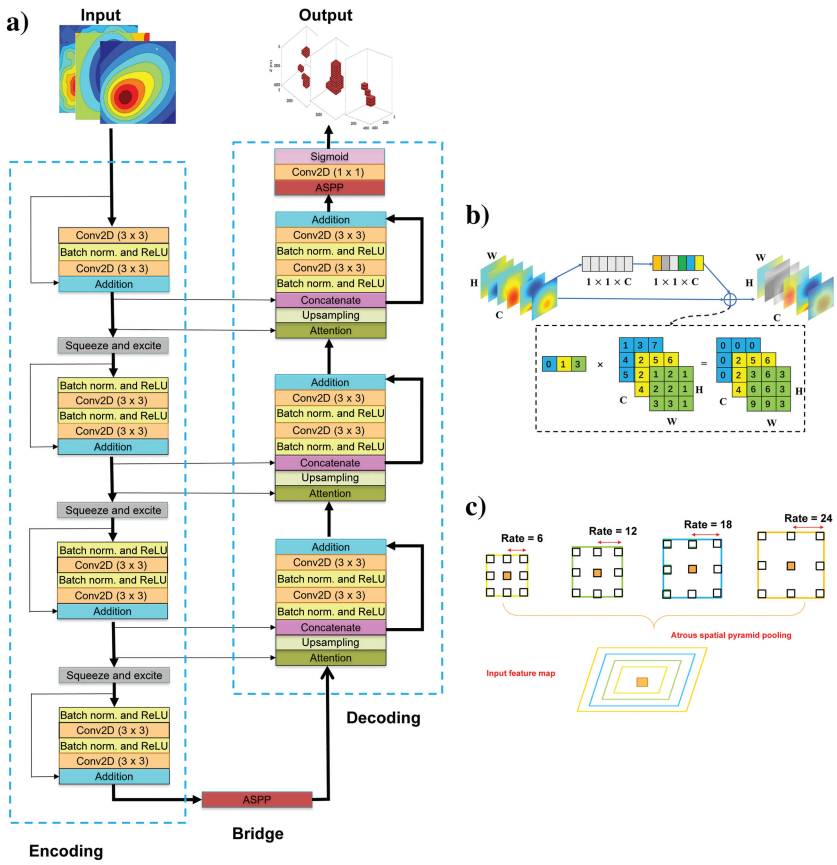

Figure 7. (a–c) Encoder-decoder structure of the ResU-Net++ network comprising a stem block, four encoder blocks, ASPP modules, and three decoder blocks. It incorporates features such as residual blocks and S-E modules; notably, it integrates residual modules within the encoding and decoding sections (highlighted by the dashed black rectangles) (modified from Jha et al., 2019).

Downloaded from http://pubs.geoscienceworld.org/seg/geophysics/article-pdf/89/5/G93/6947062/geo-2023-0551.1.pdf
by Univ Utah Marriott Library user

ResU-Net++ network

The ResU-Net++ network marks a significant evolution in deep-learning architectures, effectively combining the strengths of residual connections and the U-Net structure. This advanced network enhances the traditional R2U-Net by integrating a normalization layer within its convolutional layers, thereby creating a more refined, recurrent residual unit. This innovation significantly boosts the network's feature extraction and information transfer capabilities, enabling it to adeptly manage local and global image features, thereby elevating segmentation accuracy and robustness.

Figure 7a shows the comprehensive structure of the ResU-Net++ network, featuring a stem block followed by four encoder blocks, an ASPP module, and three decoder blocks. These components include residual blocks and attention blocks to enhance detail capture and noise reduction. Each encoder block, shown in the left-side gray section of Figure 7b, contains a residual unit paired with an S-E module (detailed in Figure 7b). This module boosts crucial gravity map features by increasing the weight of the informative channels while reducing less relevant data, thereby optimizing feature representation. Detailed information about the AG module is provided in Appendix B. The decoder blocks, detailed in the right-side gray section, combine the attention mechanisms with upsampling and concatenation processes to preserve critical information through residual connections, enhancing the predictive performance of the network.

To address the challenges, such as increasing training errors and gradient dispersion or explosion associated with deeper networks, ResU-Net++ uses improved, recurrent, residual units in the encoder and decoder blocks. These units consist of two consecutive convolution blocks that include a batch normalization (Batch Norm or BN) layer and a ReLU layer, which streamline the training process and ensure consistent information flow through the network. This structure not only simplifies training but also enhances the network's ability to accurately predict and model complex geophysical structures, outperforming traditional deep-learning models.

In addition to classical pooling mechanisms, such as max pooling and average pooling which are used to reduce the spatial dimensions of feature maps, the ASPP module introduces a novel approach to maintain spatial resolution. By implementing dilated convolutions, the ASPP module allows for varied contextual information processing from the encoder to the decoder at different scales without losing the original input's resolution. This capability is crucial for accurately capturing narrow geologic features such as strata, faults, and fractures often seen in geophysical data. The ASPP module, using spatial pyramid pooling techniques, performs multiscale sampling of gravity data features, enhancing the preservation of detailed gravitational data. Each dilation rate (Figure 7c) in the ASPP module adjusts the convolution kernel size, allowing the network to capture a broad range of scale information effectively. A detailed description of the ASPP module is given in Appendix C.

Finally, the network's output is refined through an ASPP module before being processed by a 1×1 convolution with a sigmoid activation function to produce the final model image. This output is then integrated into a fully connected feedforward 3D mapping layer, which correlates the subsurface geology with the observed gravity variations based on the network's training on supervised learning labels. This training encapsulates the relationships between the observed gravity anomalies and the density variations within the inversion domain, enabling the network to accurately predict the underground density models. The efficacy and comparative performance of the four networks, including ResU-Net++, are systematically summarized in Table 1, which organizes the module types across the four networks, indicating the presence of specific modules with an "**X**."

Table 1 highlights the distinct configurations and functionalities:

1) Nested U-Net uses "nested Structures" and residual unit (labeled as "Unit") modules. These components effectively decrease the size of the feature map while simultaneously extracting local and global information from gravity images. This dual approach ensures comprehensive analysis of the data.
2) R2U-Net builds upon the basic capabilities of the residual unit by incorporating recurrent connections (denoted as "Re." in Table 1) into the "Unit". This enhancement enriches the network's capacity for feature representation and facilitates the transmission of contextual information, making it adept at handling complex data structures.
3) AttU-Net features the "AG module", which excels in filtering out irrelevant data and enhancing the efficiency of feature mapping. This module prioritizes significant information within the gravity data, ensuring that the network focuses on the most pertinent features.
4) ResU-Net++ advances the "Unit+Re." configuration by adding a Batch Norm layer (designated as "Unit+Re.+BN."), which ensures stability and reliability in feature representation across different layers, thus boosting the overall capacity of the network to interpret and represent features accurately. Similar to AttU-Net, ResU-Net++ uses the "S-E module" to amplify essential features in gravity maps by assigning greater weights to significant channels while reducing noise and less critical elements. Moreover, the

Table 1. Comparison of the four main feature modules' distribution across four networks.

Networks	Nested structures		Residual module		Attention		mechanisms
	Unit	Unit + Re.	ASPP module	Unit + Re. + BN	AG	S-E	
Nested U-Net	X	X					
R2U-Net		X	X				
AttU-Net (see Appendix A)					X		
ResU-Net++ (see Appendices B and C)		X	X	X		X	X

Downloaded from http://pubs.geoscienceworld.org/seg/geophysics/article-pdf/89/5/G93/6947062/geo-2023-0551.1.pdf
by Univ Utah Marriott Library user

introduction of the "ASPP module" in ResU-Net++ uses varying dilation rates to capture semantic information at multiple scales. This feature allows the network to more effectively discern local and global features in images, thereby enhancing the accuracy and robustness of the segmentation tasks. This multiscale approach is pivotal for detailed and precise geophysical data analysis.

In the upcoming simulation and verification stages, we will use these four networks to reconstruct the amplitude and shape of underground abnormal-density bodies. This initiative will allow us to comprehensively assess the networks' effectiveness in accurately representing the physical properties of subsurface structures. This evaluation is crucial for advancing our understanding of how these deep-learning architectures perform in real-world geologic scenarios.

Validation

To validate the robustness of the various U-Net-based networks, this study uses normalized misfit E, to portray the gravity observation loss during training. The specific formula for this loss is as follows:

$$E = \frac{\sqrt{\sum_1^N (g_n^{\text{obs}} - g_n^{\text{pre}})^2}}{\sqrt{\sum_1^N (g_n^{\text{obs}})^2}}, \tag{1}$$

where N is the total number of observed points, g^{obs} denotes the theoretical observed gravity data, and g^{pre} represents the predicted gravity data.

SYNTHETIC STUDY

To assess the network's effectiveness in feature detection, we develop two straightforward simulation models. Figures 8 and 9 show visual depictions of a contact assembly model, featuring a rectangular and a trapezoidal anomaly and a separated, combined model comprised of five block anomalies, respectively, which are targeted for predictive analysis. Both models maintain a uniform density of 1.0 g/cm^3, as reported by Huang et al. (2021) and Wang et al. (2024). The observation field spans 0–4000 m along the x-axis and 0–4000 m along the y-axis, with an interval of 200 m between data points, culminating in a total of 441 data points to evaluate the vertical component of gravity. The inversion domain, conceived in three dimensions, was partitioned into 8000 cubic cells (20 m × 20 m × 20 m), each with side lengths of 200 m. For improved legibility, all 3D perspectives are in portions with a density exceeding 0.5 g/cm^3.

Results and interpretation

Contact assembly model

Figure 10 shows a comparative analysis, presenting the contact assembly model (Figure 10a) against the inversion outcomes using regularized focusing conjugate gradient (RCG) inversion (Figure 10b) and various networks: the nested U-Net (Figure 10c), R2U-Net (Figure 10d), AttU-Net (Figure 10e), and ResU-Net++ (Figure 10f). In Figure 10a, the first and second columns display 3D views showing horizontal sections at X = 2200 m and cross sections at Y = 1000 m, respectively, and the third column shows the observed gravity field. Figure 10b–10f shows the reconstructed densities at these sections, with the third column displaying the predicted gravity field for each method.

It is evident from Figure 10b that the shape reconstructed via regularized focusing RCG shows a more divergent characteristic and achieves lower amplitude recovery. The nested U-Net's results (Figure 10c) closely mimic the actual model, albeit with slight variations in residual density around the anomaly edges. R2U-Net (Figure 10d) improves the alignment of the recovered shapes, particularly in defining clearer boundaries at the cube's edges. AttU-Net (Figure 10e) accurately predicts the density values, closely reflecting the theoretical predictions, particularly evident in the lateral views. Yet, subtle low-density areas within the trapezoidal anomaly remain a challenge. ResU-Net++ (Figure 10f) exhibits the best inversion modeling performance, with density values that closely replicate the actual model, leading to superior inversion results. Figure 11 depicts the mean-squared error (MSE) loss curves for the four U-Net variants, showing a clear convergence in the loss functions as the

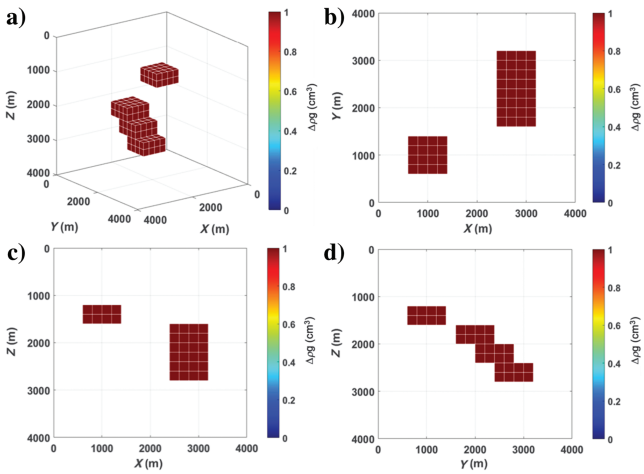

Figure 8. (a) The 3D view of the contact assembly model, (b) the x-z view, (c) the y-z view, and (d) the x-y view.

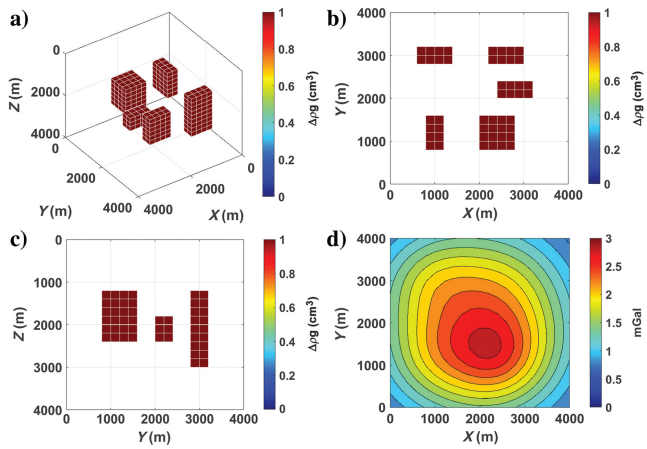

Figure 9. (a) The 3D view of the separated combined model, (b) x-z view, (c) y-z view, and (d) gravity anomaly.

Downloaded from http://pubs.geoscienceworld.org/seg/geophysics/article-pdf/89/5/G93/6947062/geo-2023-0551.1.pdf
by Univ Utah Marriott Library user

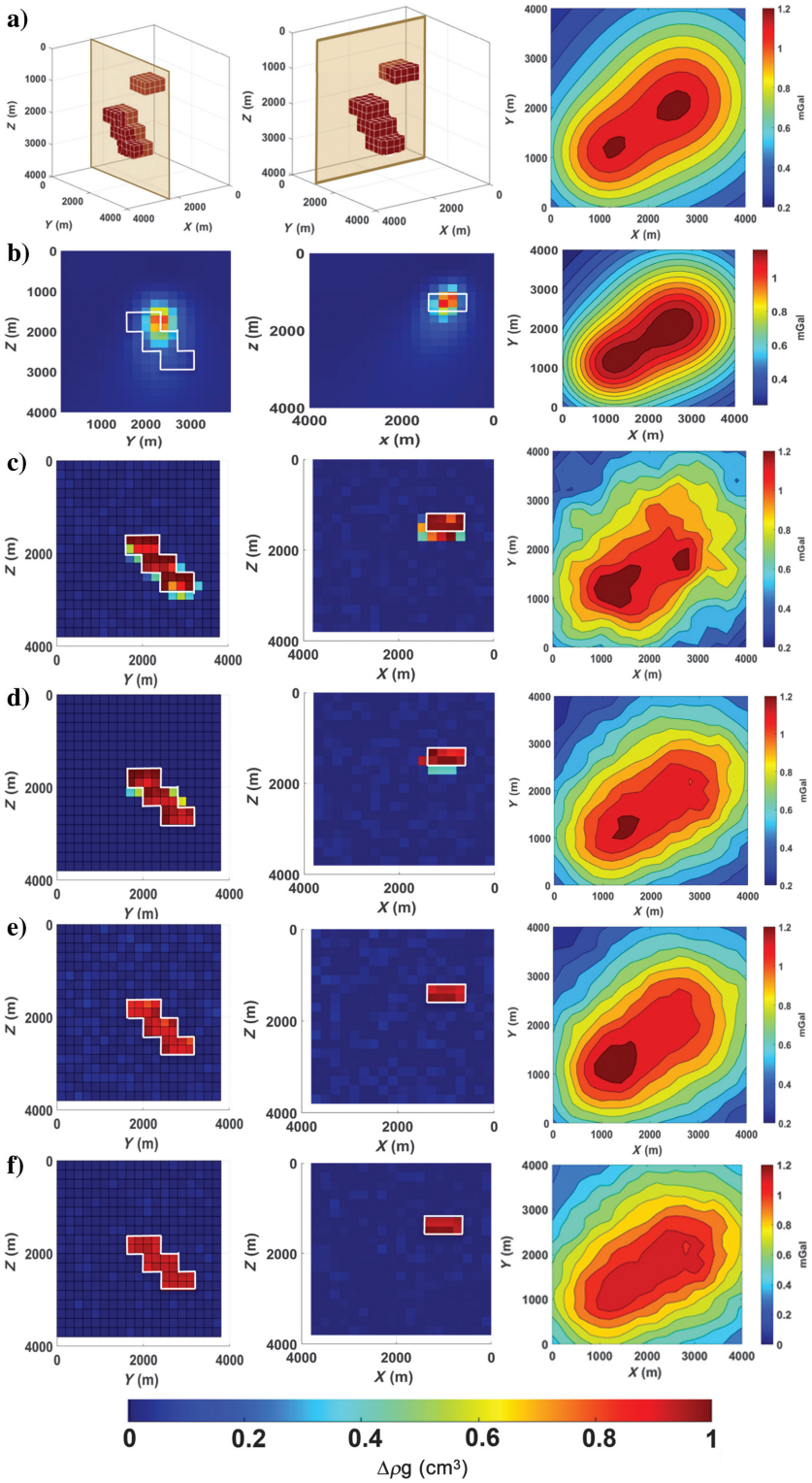

Figure 10. Comparison of the inversion results of the contact assembly model with noise-free (a) initial model, (b) model recovered by regularized focusing gravity inversion, (c) model recovered by the nested U-Net network, (d) model recovered by the R2U-Net network, (e) model recovered by the AttU-Net network, and (f) model recovered by the ResU-Net++ network.

training progresses. Notably, by epoch 100, all four networks demonstrate convergence in their loss functions. This convergence signifies the successful minimization of the difference between the predicted and actual values, indicating that the models have reached a stable state in their training process.

Figure 12 shows the misfit analysis for the four networks. It is evident from the data that the misfit values predicted by all four networks remain under 5%. Notably, the ResU-Net++ network exhibits the lowest misfit percentage, underscoring its superior predictive accuracy compared with the others. Due to the striking similarity between the misfit map of the focusing RCG inversion and that of the ResU-Net++, it has not been included in this paper for brevity.

To verify the robustness of ResU-Net++ against noise, we added Gaussian random noise at different levels to the gravity data and performed density predictions. Figure 13a–13c shows the prediction results without noise, with 5% noise, and with 10% noise, respectively, illustrating that the network maintains a close alignment between the observed and predicted gravity fields across all noise levels.

The relationship between the complexity of a network and its training duration is meticulously outlined in Table 2, highlighting that more sophisticated networks necessitate longer training periods. Specifically, (1) the R2U-Net, the simplest in this study with more than 51 million neurons, boasts the shortest training duration of 10 min, making it ideal for scenarios requiring rapid model training. (2) The Nested U-Net, with almost 72 million neurons, requires a slightly longer training time of 12 min, reflecting a modest increase in complexity and enhanced capability for capturing detailed features. (3) The AttU-Net, significantly more complex with more than 100 million neurons, demands 15 min of training time. (4) The ResU-Net++, the most intricate model evaluated, with more than 102 million neurons, necessitates the longest training period of 16 min. This extended training time is indicative of its superior capacity for detailed data processing and accuracy, essential for complex gravity inversion tasks. For a comprehensive understanding of the networks' configurations, see Table 3, which details the hyperparameters used during network training.

Separated combined model (five block anomalies)

Similarly, Figure 14 shows a visual comparison of the second synthetic model (illustrated in Figure 14a) against the inversion results from focused RCG inversion (Figure 14b) and the four networks: the nested U-Net (Figure 14c),

Downloaded from http://pubs.geoscienceworld.org/seg/geophysics/article-pdf/89/5/G93/6947062/geo-2023-0551.1.pdf
by Univ Utah Marriott Library user

R2U-Net (Figure 14d), AttU-Net (Figure 14e), and ResU-Net++ (Figure 14f).

In Figure 14a, the first and second columns provide 3D perspectives, featuring a horizontal section at $Z = 2000$ m and a cross section at $X = 2400$ m, respectively. The third column displays the observed gravity field. In Figure 14b–14f, the first and second columns depict the reconstructed density at the same horizontal and cross sections, respectively, whereas the third column presents the predicted gravity field, facilitating a direct comparison of the inversion outcomes across different methods.

Table 2. Number of network neurons, training time, and number of training grids.

Networks	Number of neurons	Training time (min)	Number of training grids
R2U-Net	51,354,435	10	8000
Nested U-Net	71,868,240	12	8000
AttU-Net	100,423,436	15	8000
ResU-Net++	102,174,496	16	8000

Table 3. Network training parameters.

Parameters	Values
Learning rate	0.00001
Epoch	100
Batch size	256
Dropout	0.5
Kernel size	3
Activation function	ReLU
Early stopping	200

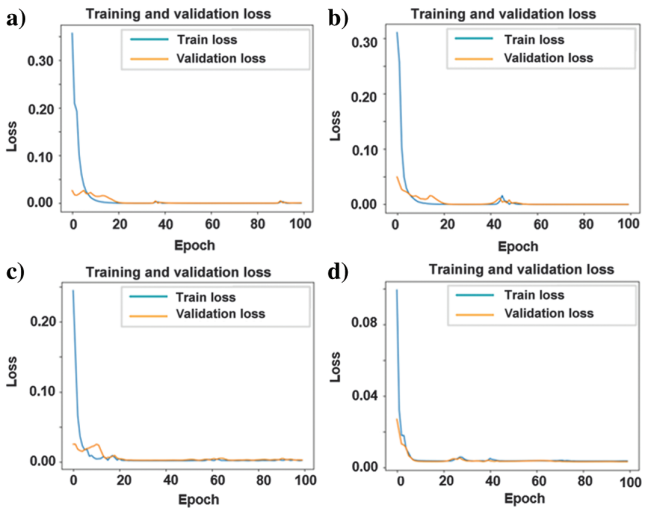

Figure 11. The MSE error diagram for (a) nested U-Net network, (b) R2U-Net network, (c) AttU-Net network, and (d) ResU-Net++ network.

It is evident that the model predictions by nested U-Net (Figure 14c) closely resemble the actual model (Figure 14a), though with slight deviations in the residual density around the edges of the five rectangular blocks. Upon examining the R2U-Net network (Figure 14d), the alignment of the reconstructed shape with the actual model shows enhanced accuracy, particularly in the definition of the boundaries and the clarity of the residual densities along the sides of the rectangular blocks. The AttU-Net network (Figure 14e) showcases impressively accurate predicted density values, particularly from the *Y*-*Z* perspectives, closely matching the theoretical expectations. This highlights the progress deep-learning networks have made in capturing edge cells, a feature initially overlooked by the nested U-Net. Nevertheless, the issue of excessive density units at the base of the blocks remains unresolved. In contrast, the ResU-Net++ network (Figure 14f) outperforms in inversion modeling, precisely replicating the actual model's density values and delivering an exemplary inversion result. In addition, compared with the focused RCG inversion shown in Figure 14b, it becomes clear that traditional methods struggle to accurately reconstruct the shape and amplitude of the five anomalous bodies, predominantly due to volume effects.

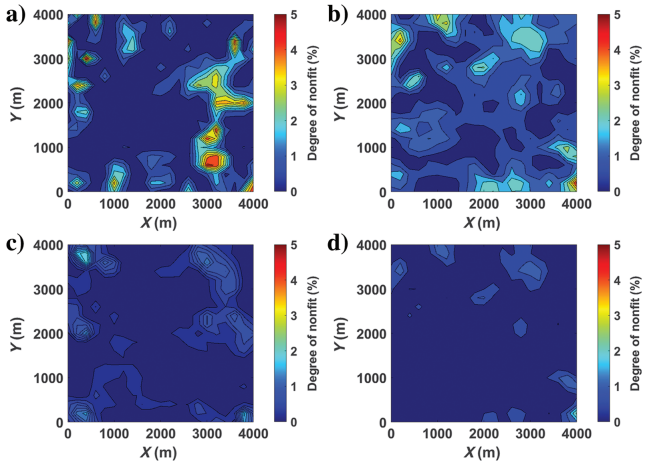

Figure 12. Comparison of the misfit behaviors of the contact assembly model by the (a) nested U-Net, (b) R2U-Net, (c) AttU-Net, and (d) ResU-Net++.

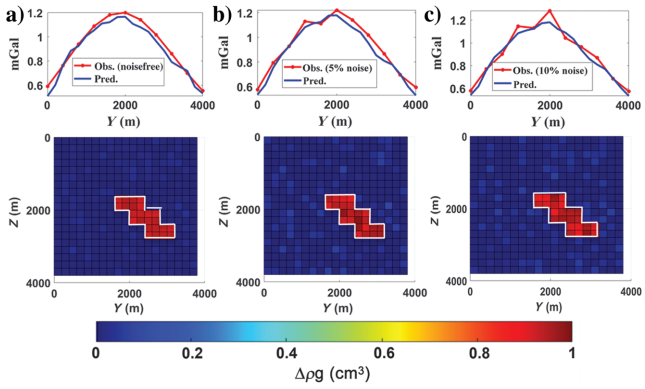

Figure 13. Comparison of the inversion results by ResU-Net++ under various noise conditions. Gravity field fitting diagram, density prediction, and form recovery with (a) no noise, (b) 5% Gaussian noise, and (c) 10% Gaussian noise, respectively.

Downloaded from http://pubs.geoscienceworld.org/seg/geophysics/article-pdf/89/5/G93/6947062/geo-2023-0551.1.pdf
by Univ Utah Marriott Library user

To assess the network's robustness against noise in various models, the prediction outcomes presented here include an addition of 5% Gaussian noise. Figure 15 shows the misfit degree chart for the field predictions made by the four networks. The chart reveals that all the networks sustain a misfit below 5%, with ResU-Net++ showcasing the lowest misfit degree. This indicates that ResU-Net++ surpasses the other networks in terms of prediction accuracy.

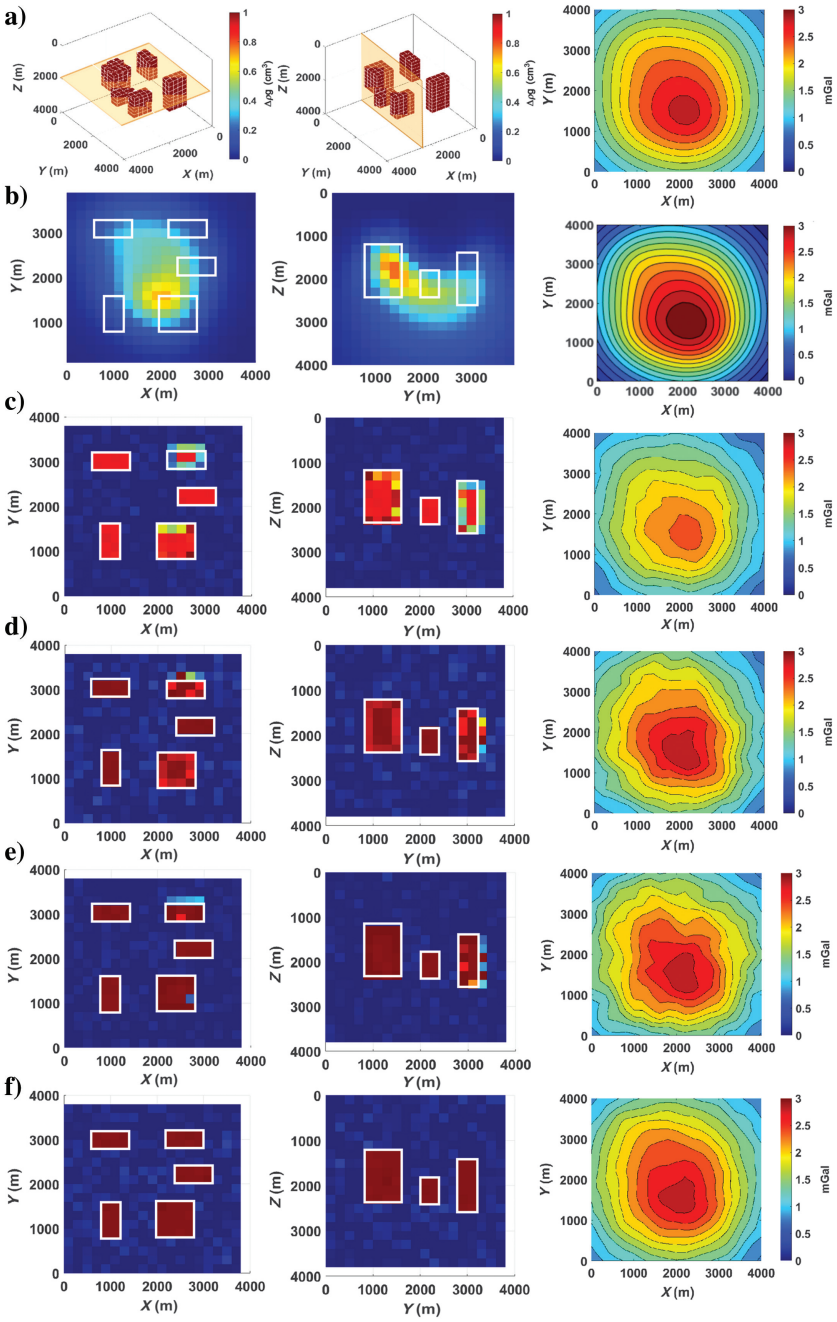

Figure 14. Comparison of the inversion results of the separated combined model with noise-free (a) initial model, (b) model recovered by regularized focusing gravity inversion, (c) model recovered by the nested U-Net network, (d) model recovered by the R2U-Net network, (e) model recovered by the AttU-Net network, and (f) model recovered by the ResU-Net++ network.

To provide a more quantitative evaluation of the inversion results from the four networks, we computed the field map fitting errors for each network using equation 1, as shown in Table 4. A lower field value fitting error indicates a better alignment between the predicted and observed field maps, reflecting a network's enhanced predictive capability. Conversely, a higher error suggests a weaker prediction performance. The data in Table 4 show that the field value fitting error for all the networks is under 10%, indicating that each network achieves a commendable level of predictive accuracy. Notably, the AttU-Net and ResU-Net++ networks exhibit field value fitting errors below 5%, signaling more accurate predictions. Specifically, the ResU-Net++ network has the lowest field value fitting error, underscoring its superior performance in model validation trials. This outcome emphasizes the ResU-Net++ network's effectiveness in retaining and processing essential original information.

To address the challenge of overfitting, our strategy involves a detailed analysis of the loss curve. Indicators of overfitting include a consistent decline in the training error alongside a stagnating or increasing validation error, which often suggests that the model, although performing well on the training data, fails to replicate these results on the validation data. In tackling the complex demands of gravity inversion, we have implemented several countermeasures to prevent overfitting. These include the use of dropout, early stopping, learning rate adjustment, and weight regularization. Each of these techniques is deliberately selected and applied to improve the model's generalization ability and robustness, ensuring its reliability and efficacy in various testing environments.

CASE STUDY

Geologic characteristics of the area of a 3D marine gravity survey

A full tensor gradiometry (FTG) survey was conducted in the Nordkapp Basin, located offshore Norway in the Barents Sea, as shown in Figure 16a. This basin is divided into the southwestern part (SWP) and the northeastern part (NEP). The SWP, particularly in the Obelix survey area, features a narrow geologic formation that extends 150 km in length and ranges from 25 to 50 km in width, with a northeast orientation. This area is notable for containing more than 17 complex salt diapirs, which are significant geologic structures within this subbasin (refer to Figure 16b). In contrast, the NEP subbasin measures approximately 200 km in length and 50–70 km in width and is home to more than 16 salt formations. Hydrocarbon exploration in the Nordkapp Basin began in the 1980s, with three wells drilled to date, all located at the

Downloaded from http://pubs.geoscienceworld.org/seg/geophysics/article-pdf/89/5/G93/6947062/geo-2023-0551.1.pdf
by Univ Utah Marriott Library user

basin's periphery. Recent geologic and geophysical surveys, coupled with the discoveries of hydrocarbon deposits in adjacent wells, suggest that the Nordkapp Basin may hold untapped hydrocarbon reservoirs.

The primary geologic targets within the Nordkapp Basin are the F2 salt diapirs, identifiable by their lack of clearly delineated seismic horizons, as shown in Figure 17. As seismic techniques and structural interpretations advance, mapping the salt structures in the basin has become increasingly complex. Salt stocks, originally characterized by vertical sides, have evolved into formations with expansive diapiric overhangs supported by narrow stems.

However, the seismic depth migration images along profiles K-K′ (Figure 18a) and S-S′ (Figure 18b) often exhibit distortions due to the properties of the salt and the underconstrained inversion models of the salt isopach. These challenges limit the effectiveness of seismic tools in accurately mapping the base of the salt formations. In response, the FTG survey provides additional data that help in assessing these complex salt overhang structures. Due to its sensitivity to geologic anomalies with significant density variations, the FTG methodology is particularly effective in tackling such challenges. Statoil offers two types of interpretations for the salt base along S-S′ (Figure 18b): one derived from the seismic data, depicted by a solid purple line, and another based on the FTG data, shown by a dashed red line (Xu et al., 2020). These dual interpretations will be used to identify and validate the inversion results.

The specific challenge addressed here pertains to the difficulties in interpreting salt structures using seismic data, thus necessitating

Table 4. Comparison of the misfit behavior corresponding to the four networks.

U-Net-based networks	Misfit behavior 1	Misfit behavior 2
Nested U-Net	0.0905	0.0825
R2U-Net	0.0900	0.0702
AttU-Net	0.0434	0.0496
ResU-Net++	0.0404	0.0366

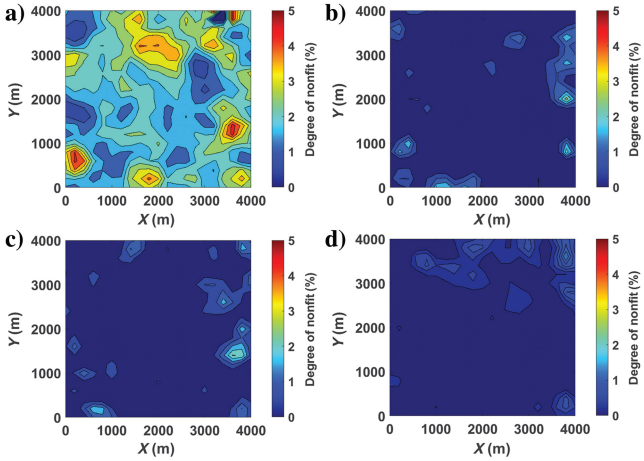

Figure 15. Comparison of the misfit behaviors of the separated combined model by the (a) nested U-Net, (b) R2U-Net, (c) AttU-Net, and (d) ResU-Net++.

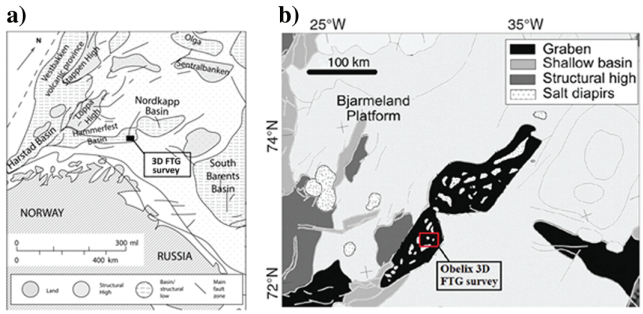

Figure 16. (a) Main structural elements in the Barents Sea area, location of the Nordkapp Basin and 3D FTG survey (modified from Johansen et al., 1993). (b) Simplified structural map of the Nordkapp Basin showing salt diapirs and main fault zones. Black zones show subcrops of the diapirs at or near the Pliocene-Pleistocene unconformity (modified from Zhdanov and Lin, 2017).

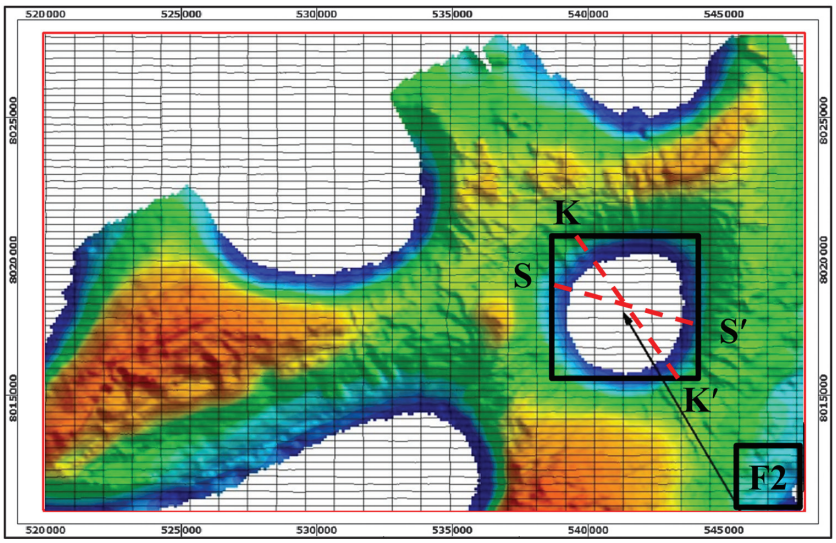

Figure 17. Obelix 3D FTG survey grid with seismic horizons. The main geologic targets are the salt diapirs G2 and F2, which are manifested by the absence of well-resolved seismic horizons. The area marked with the solid red line is the original FTG survey grid. The subset marked with a solid black line of the original FTG data focuses on the F2 salt diapir areas. The seismic survey lines K-K′ and S-S′ are uniformly marked with the dashed red lines.

Downloaded from http://pubs.geoscienceworld.org/seg/geophysics/article-pdf/89/5/G93/6947062/geo-2023-0551.1.pdf
by Univ Utah Marriott Library user

precise 3D inversion of the FTG data. Numerous studies have focused on achieving sharp boundary inversion of the FTG data in the Nordkapp Basin through focusing regularization techniques (Zhdanov and Lin, 2017; Xu et al., 2020; Tao et al., 2021; Tu and Zhdanov, 2022). This paper presents the preliminary results from using the ResU-Net++ network, which effectively connects the labels, geologic models, trained data, and forecasted outcomes to delineate the sharp density contrasts between the salt structures and the surrounding host rock.

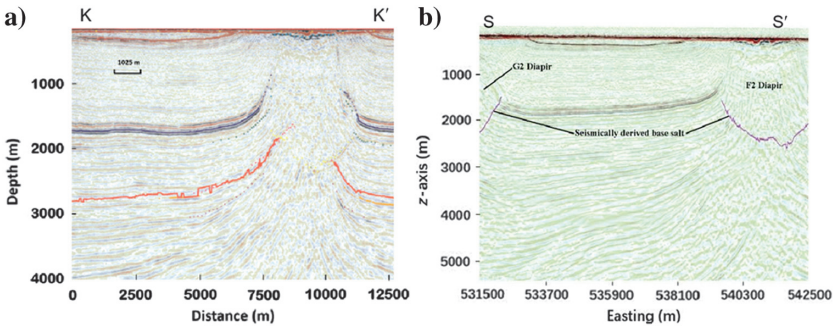

Figure 18. Seismic depth migrated profile from a 3D survey showing the salt feature F2 and typical imaging ambiguity of the high-resolution seismic along (a) K-K′ and (b) S-S′ (modified from Xu et al., 2020).

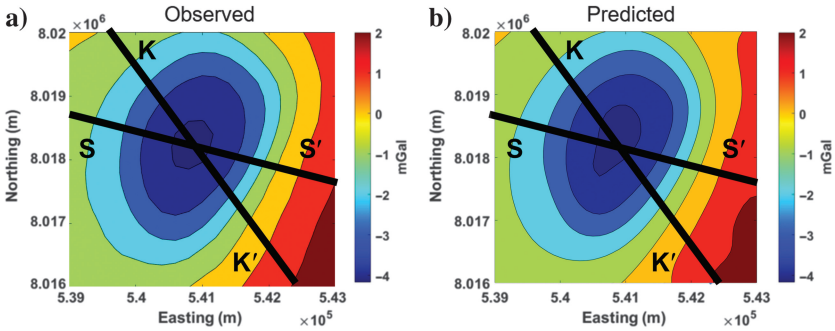

Figure 19. Comparison of (a) the observed gravity data and (b) predicted gravity data based on ResU-Net++.

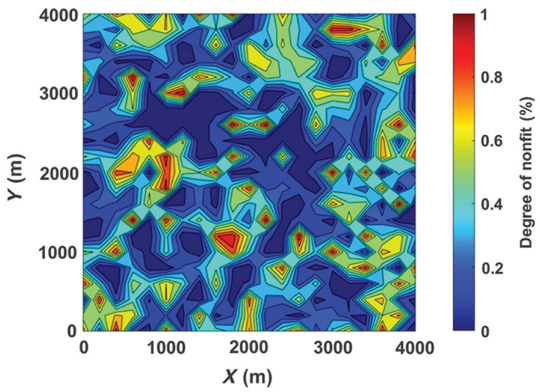

Figure 20. Data misfit between the observed and predicted gravity data.

Results and interpretation

In our study, as detailed in Table 1, the ResU-Net++ network incorporates a comprehensive array of modules found in nested U-Net, R2U-Net, and AttU-Net. This includes elements such as residual connections and attention mechanisms, providing ResU-Net++ with a robust structure and theoretically enhanced prediction capabilities. Our simulation tests, specifically with model 1 (the contact assembly model) and model 2 (the five separated combined model), have shown that ResU-Net++ surpasses traditional inversion methods and the other three networks in terms of clarity in the morphology and amplitude recovery of the inversion model. It also consistently exhibits the smallest error in field map recovery. Based on these strong performance indicators, we chose to use the ResU-Net++ network for processing actual data, leveraging its superior performance demonstrated in the simulation tests.

Focusing on the primary geologic objective, the F2 salt diapir, we isolated a subset of the FTG data from the initial data set to specifically target the regions highlighted by the F2 marker. We present a vertical cross-sectional comparison of the inversion results alongside the S-S′ and K-K′ seismic profiles. In this preliminary application of the ResU-Net++ network, the vertical component of the gravity field (g_z) was used for the inversion process. The designated inversion area spans a 4 km cube in the east–west (x-axis) and north–south (y-axis) dimensions and extends to a depth of 4 km (z-axis). This inversion volume was divided into 8000 cubic cells, each measuring 200 m × 200 m × 200 m.

Figure 19a shows the zone of the observed data used for the inversion. The multiscale module does not impose any constraints on either the size of the observation surface or the number of observation points. Figure 19b shows the forecasted observed gravity data map, generated through the application of the ResU-Net++ network, exhibiting a high degree of similarity with the genuine observed data. In addition, Figure 20 shows the degree of nonfitting error corresponding to Figure 19a and 19b. The error is less than 1%, illustrating that the ResU-Net++'s predictions for the underground salt dome and surrounding rock closely align with the observed gravity field in the data space. This indicates a high degree of accuracy in the network's predictive capabilities.

To evaluate the precision of our results, we compared the density inversions from the ResU-Net++ (Figures 21a and 22a) and the traditional focusing RCG inversion (Figures 21b and 22b) along the seismic profiles K-K′ (Figure 21) and S-S′ (Figure 22). The conventional inversion method's reconstructions of the salt dome geometries display divergent contours with smoother less-defined boundaries. In contrast, ResU-Net++ achieves sharper boundary delineations that align closely with the seismic interpretation data. These comparisons highlight ResU-Net++'s effectiveness and affirm the superiority of deep-learning approaches in delivering more precise predictive outcomes.

Downloaded from http://pubs.geoscienceworld.org/seg/geophysics/article-pdf/89/5/G93/6947062/geo-2023-0551.1.pdf
by Univ Utah Marriott Library user

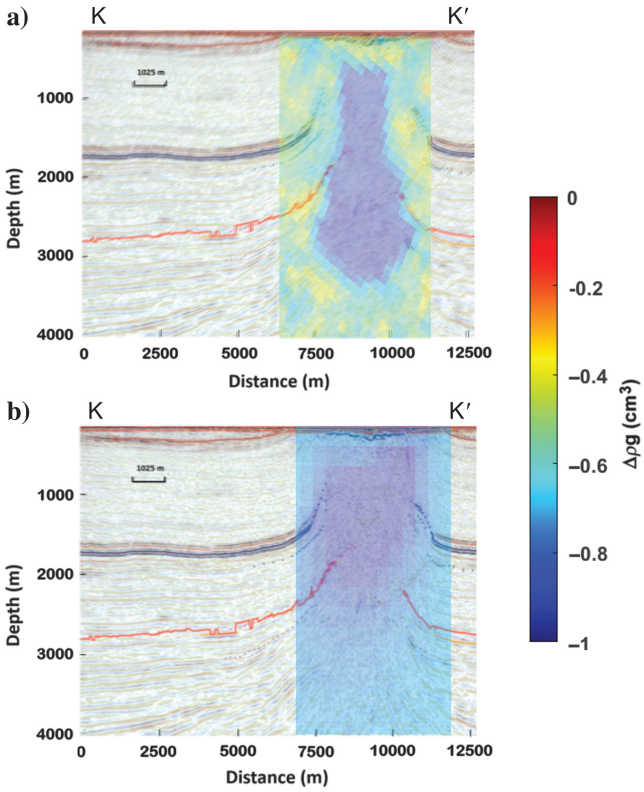

Figure 21. The comparison of the anomalous density recovered by (a) the ResU-Net++ network model and (b) focusing the RCG inversion along the seismic line profile K-K′.

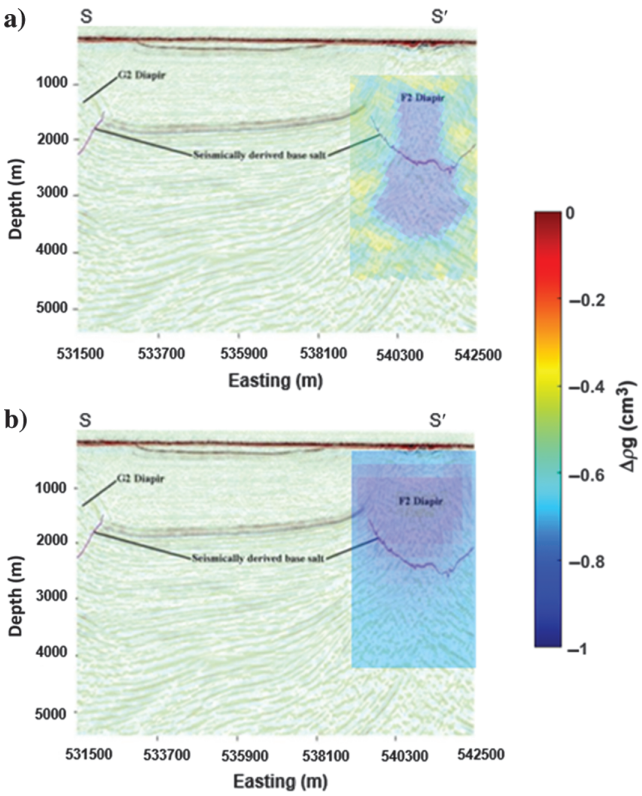

Figure 22. The comparison of the anomalous density recovered by (a) the ResU-Net++ network model and (b) focusing the RCG inversion along the seismic line profile S-S′.

CONCLUSION

Gravity-based inversion is crucial in geophysical research, aiding in identifying geologic anomalies, mapping rock formations, and extracting resources such as oil and minerals. However, traditional gravity inversion methods face challenges such as the volumetric effects of gravity fields, underdetermined matrices, and the management of large ill-posed matrices. Furthermore, unsupervised learning methods often struggle with overfitting and complexities in interpreting gravity data. In the realm of U-Net-based architectures, each presents distinct challenges and benefits. For instance, the nested U-Net is robust but requires many parameters, leading to longer training times. R2U-Net, with its implicit attention mechanism, is limited in adjusting geophysical feature weights dynamically. Conversely, AttU-Net, lacking residual connections, faces potential issues with gradient vanishing.

This paper delineates the training methodologies, principles, and functions of the primary feature modules of nested U-Net, R2U-Net, AttU-Net, and ResU-Net++. It explores how these modules are distributed across the networks and evaluates their effectiveness compared with traditional focusing RCG inversion for density anomaly reconstruction. Our synthetic studies indicate that although the RCG technique struggles with low amplitude recovery and divergent geometric representations, the nested U-Net shows a close resemblance to the actual model but tends to produce redundant density units. R2U-Net improves the model alignment but struggles with slight redundancies, and AttU-Net excels in density prediction despite the challenges with low-density areas. Remarkably, ResU-Net++ outperforms all in inversion modeling, replicating density values more accurately and exhibiting the lowest misfit percentage, showcasing its exceptional predictive accuracy and robustness against noise. In practical scenarios, ResU-Net++'s reconstructed model of the F2 salt diapir in the Nordkapp Basin displays sharply defined boundaries and closely mirrors seismic interpretations, underscoring its capability in geophysical data analysis, structural reconstruction, and inversion tasks.

ACKNOWLEDGMENTS

The authors would like to thank the Key Laboratory of Earth Exploration and Information Techniques of the Ministry of Education, Chengdu University of Technology and College of Geophysics, Chengdu University of Technology, and Changchun University of Science and Technology. They also acknowledge the Consortium for Electromagnetic Modeling and Inversion (CEMI), University of Utah, Salt Lake City, UT, USA, for providing the gravity and related geophysical data. The FTG data were collected by BellGeospace and made available by Equinor (formerly Statoil). This work was financially supported by the National Key Research and Development Program of China (no. 2022YFC3003204), the National Natural Science Foundation of China (41930112 and 42274132), and the Natural Science Foundation of Sichuan Province (no. 24NSFSC1864).

Downloaded from http://pubs.geoscienceworld.org/seg/geophysics/article-pdf/89/5/G93/6947062/geo-2023-0551.1.pdf
by Univ Utah Marriott Library user

DATA AND MATERIALS AVAILABILITY

Data associated with this research are confidential and cannot be released.

APPENDIX A

DERIVATION FORMULA OF AG MODULE

The output of AG (Figure 6b), defined as $\hat{x}_i^l$, is the element-wise multiplication of input feature maps x_i^l and attention coefficients α_i^l as

$$\hat{x}_i^l = x_i^l \cdot \alpha_i^l, \tag{A-1}$$

where α_i^l can be expressed as

$$\alpha_i^l = \sigma_2(q_{\text{att}}^l), \tag{A-2}$$

where $\sigma_2(\dots)$ corresponds to the sigmoid activation function and q_{att}^l is an inner function in a compound function α_i^l shown in equation A-2 as

$$q_{\text{att}}^l = \psi^T(\sigma_1(W_x^T x_i^l + W_g^T g_i + b_g)) + b_\psi, \tag{A-3}$$

where $\psi \in \mathbb{R}^{F_{\text{int}} \times 1}$ represents the linear transformations computed using channel-wise $1 \times 1 \times 1$ convolutions for the input tensors; $\sigma_1(\dots)$ corresponds to the ReLU activation function; $W_x \in \mathbb{R}^{F_i \times F_{\text{int}}}$ and $W_g \in \mathbb{R}^{F_g \times F_{\text{int}}}$ are defined as the corresponding weighting for x_i^l and g_i, respectively; $b_g \in \mathbb{R}^{F_{\text{int}}}$ and $b_\psi \in \mathbb{R}$ are defined as the corresponding bias terms; and T represents the matrix transpose.

APPENDIX B

DERIVATION FORMULA OF SE MODULE

The S-E operation compresses the input $U \in \mathbb{R}^{H \times W \times C}$ into a vector $F_{sq}(u_c)$ through global pooling, as shown in equation B-1 as

$$F_{sq}(u_c) = \frac{1}{H \times W} \sum_{i=1}^{H} \sum_{j=1}^{W} u_c(i, j), \tag{B-1}$$

where $u_c(i, j)$ represents the cth element in the input $U \in \mathbb{R}^{H \times W \times C}$ and H and W represent the numbers of the row and column of the extracted gravity input data by convolution throughout the designed number of channels (C), respectively.

To discern the channel-level dependencies, which involve giving larger weights to the crucial feature maps within a feature channel to emphasize the key elements while shrinking the unimportant ones during the feature extraction, an excitation operation is used. This operation produces a weight value for each feature channel through the implementation of two fully connected layers.

The resulting output is derived by multiplying each channel by its associated channel weight. The output of this mapping operation is given by

$$s = F_{ex}(z, W) = \sigma(W_2 \delta(W_1 z)), \tag{B-2}$$

where z represents a single 2D tensor as an element of $X \in \mathbb{R}^{H \times W}$ of the input $U \in \mathbb{R}^{H \times W \times C}$ and σ represents the sigmoid function. The weight matrices are denoted as $W_1 \in \mathbb{R}^{(C/r) \times c}$ and $W_2 \in \mathbb{R}^{(C/r) \times c}$, where the hyperparameter r dictates the compression ratio of the parameters in the initial fully connected layer.

APPENDIX C

THE KERNEL IN THE ASPP MODULE

In the structure of the ASPP module (Figure 7c), the size of the equivalent convolution kernel (i.e., the receptive field) of an expansive convolution is as follows:

$$\text{kernel} = k + 2(k - 1)(\text{rate} - 1), \tag{C-1}$$

where k is the original convolution kernel size (e.g., 3×3 in Figure 7c) and rate is the expansion coefficient. The output size obtained after the convolution is defined as $\text{out} = ((\text{input} - \text{kernel} + 2 \times \text{padding})/\text{stride})$, where out denotes the output size and input denotes the input size. The stride represents the length of a stride. The padding operation addresses the information loss near the image boundary following each convolution operation. This is achieved by substituting the absent boundary sections with zero.

REFERENCES

Alaofin, O. T., 2022, Application of gravity data for hydrocarbon exploration using machine learning assisted workflow: Louisiana State University and Agricultural & Mechanical College.

Alom, M. Z., M. Hasan, C. Yakopcic, T. M. Taha, and V. K. Asari, 2018, Recurrent residual convolutional neural network based on U-Net (R2U-Net) for medical image segmentation: arXiv preprint, doi: 10.48550/arXiv.1802.06955.

Amiramjadi, M., R. Plougonven, A. R. Mohebalhojeh, and M. Mirzaei, 2023, Using machine learning to estimate nonorographic gravity wave characteristics at source levels: Journal of the Atmospheric Sciences, **80**, 419–440, doi: 10.1175/JAS-D-22-0021.1.

Annan, R. F., and X. Wan, 2022, Recovering bathymetry of the Gulf of Guinea using altimetry-derived gravity field products combined via convolutional neural network: Surveys in Geophysics, **43**, 1541–1561, doi: 10.1007/s10712-022-09720-5.

Backus, G., 1970a, Inference from inadequate and inaccurate data, I: Proceedings of the National Academy of Sciences, **65**, 1–7, doi: 10.1073/pnas.65.1.1.

Backus, G., 1970b, Inference from inadequate and inaccurate data, III: Proceedings of the National Academy of Sciences, **67**, 282–289, doi: 10.1073/pnas.67.1.282.

Backus, G., and F. Gilbert, 1968, The resolving power of gross earth data: Geophysical Journal International, **16**, 169–205 doi: 10.1111/j.1365-246X.1968.tb00216.x.

Backus, G. E., and J. F. Gilbert, 1967, Numerical applications of a formalism for geophysical inverse problems: Geophysical Journal International, **13**, 247–276, doi: 10.1111/j.1365-246X.1967.tb02159.x.

Cai, H., and M. Zhdanov, 2015, Application of Cauchy-type integrals in developing effective methods for depth-to-basement inversion of gravity and gravity gradiometry data: Geophysics, **80**, no. 2, G81–G94, doi: 10.1190/geo2014-0332.1.

Chen, H., Y. He, L. Zhang, S. Yao, W. Yang, Y. Fang, Y. Liu, and B. Gao, 2023, A landslide extraction method of channel attention mechanism U-Net network based on Sentinel-2A remote sensing images: International Journal of Digital Earth, **16**, 552–577, doi: 10.1080/17538947.2023.2177359.

Chen, X., Y. Du, Z. Liu, W. Zhao, and X. Chen, 2018, Inversion of density interfaces using the pseudo-backpropagation neural network method: Pure and Applied Geophysics, **175**, 4427–4447, doi: 10.1007/s00024-018-1889-7.

Delcey, M., Y. Cheny, and S. Kiesgen de Richter, 2023, Physics-informed neural networks for gravity currents reconstruction from limited data: Physics of Fluids, **35**, 027124, doi: 10.1063/5.0136886.

Foster, M., 1961, An application of the Wiener-Kolmogorov smoothing theory to matrix inversion: Journal of the Society for Industrial and Applied Mathematics, **9**, 387–392, doi: 10.1137/0109031.

Downloaded from http://pubs.geoscienceworld.org/seg/geophysics/article-pdf/89/5/G93/6947062/geo-2023-0551.1.pdf
by Univ Utah Marriott Library user

Franklin, J. N., 1970, Well-posed stochastic extensions of ill-posed linear problems: Journal of Mathematical Analysis and Applications, **31**, 682–716, doi: 10.1016/0022-247X(70)90017-X.
Gao, K., L. Huang, and Y. Zheng, 2021, Fault detection on seismic structural images using a nested residual U-Net: IEEE Transactions on Geoscience and Remote Sensing, **60**, 1–15, doi: 10.1109/TGRS.2021.3073840.
Gao, X.-H., and D.-N. Huang, 2017, Research on 3D focusing inversion of gravity gradient tensor data based on a conjugate gradient algorithm: Chinese Journal of Geophysics, **60**, 1571–1583, doi: 10.6038/cjg20170429.
Guan, Z.-N., J.-S. Hou, L.-P. Huang, and C.-L. Yao, 1998, Inversion of gravity and magnetic anomalies using pseduo-BP neural network method and its application: Acta Geophysica Sinica, **41**, 241–251.
He, S., H. Cai, S. Liu, J. Xie, and X. Hu, 2021, Recovering 3D basement relief using gravity data through convolutional neural networks: Journal of Geophysical Research: Solid Earth, **126**, e2021JB022611, doi: 10.1029/2021JB022611.
Huang, R., S. Liu, R. Qi, and Y. Zhang, 2021, Deep learning 3D sparse inversion of gravity data: Journal of Geophysical Research: Solid Earth, **126**, e2021JB022476, doi: 10.1029/2021JB022476.
Jackson, D. D., 1972, Interpretation of inaccurate, insufficient and inconsistent data: Geophysical Journal International, **28**, 97–109, doi: 10.1111/j.1365-246X.1972.tb06115.x.
Jha, D., P. H. Smedsrud, M. A. Riegler, D. Johansen, T. De Lange, P. Halvorsen, and H. D. Johansen, 2019, ResUNet++: An advanced architecture for medical image segmentation: IEEE International Symposium on Multimedia.
Jiang, Z., P. Tahmasebi, and Z. Mao, 2021, Deep residual U-Net convolution neural networks with autoregressive strategy for fluid flow predictions in large-scale geosystems: Advances in Water Resources, **150**, 103878, doi: 10.1016/j.advwatres.2021.103878.
Johansen, S., B. Ostisty, Y. Fedorovsky, V. Martirosjan, O. B. Christensen, S. Cheredeev, E. Ignatenko, and L. Margulis, 1993, Hydrocarbon potential in the Barents Sea region: Play distribution and potential: Norwegian Petroleum Society Special Publications, Elsevier, 273–320.
Keilis-Borok, V., and T. Yanovskaja, 1967, Inverse problems of seismology (structural review): Geophysical Journal International, **13**, 223–234, doi: 10.1111/j.1365-246X.1967.tb02156.x.
Layade, G. O., H. Edunjobi, V. Makinde, and B. Bada, 2020, Estimation of depth to Bouguer anomaly sources using Euler deconvolution techniques: Materials and Geoenvironment, **67**, 185–195, doi: 10.2478/rmzmag-2020-0016.
Leggetter, C. J., and P. C. Woodland, 1995, Maximum likelihood linear regression for speaker adaptation of continuous density hidden Markov models: Computer Speech & Language, **9**, 171–185, doi: 10.1006/csla.1995.0010.
Li, J., Z. Xu, X. Jian, M. Li, J. Li, and X. Wang, 2023, Gravity and magnetic focusing inversion in revealing the metallogenic pattern of Dahongshan copper-iron deposit in the Kangdian Area, China: IEEE Transactions on Geoscience and Remote Sensing, **61**, 1–10, doi: 10.1109/TGRS.2023.3258964.
Li, M., Y. Li, N. Wu, Y. Tian, and T. Wang, 2020, Desert seismic random noise reduction framework based on improved PSO–SVM: Acta Geodaetica Et Geophysica, **55**, 101–117, doi: 10.1007/s40328-019-00283-3.
Liang, S., X. Wang, Z. Xu, Y. Dai, Y. Wang, J. Guo, Y. Jiao, and F. Li, 2023, Steep subduction of the Indian continental mantle lithosphere beneath the eastern Himalaya revealed by gravity anomalies: Science China Earth Sciences, **66**, 1994–2010, doi: 10.1007/s11430-022-1110-y.
Liu, Q., C. Yin, Y. Su, Y. Liu, L. Wang, H. Liang, and H. Wang, 2023, Two-dimensional fast imaging of airborne EM data based on U-Net: Frontiers in Earth Science, **10**, 1082876, doi: 10.3389/feart.2022.1082876.
Liu, S., and S. Jin, 2020, 3-D gravity anomaly inversion based on improved guided fuzzy C-means clustering algorithm: Pure and Applied Geophysics, **177**, 1005–1027, doi: 10.1007/s00024-019-02306-0.
Marquardt, D. W., 1963, An algorithm for least-squares estimation of nonlinear parameters: Journal of the Society for Industrial and Applied Mathematics, **11**, 431–441, doi: 10.1137/0111030.
Marques-Silva, J., T. Gerspacher, M. Cooper, A. Ignatiev, and N. Narodytska, 2020, Explaining naive Bayes and other linear classifiers with polynomial time and delay: Advances in Neural Information Processing Systems, 20590–20600
Montesinos, F., J. Arnoso, and R. Vieira, 2005, Using a genetic algorithm for 3-D inversion of gravity data in Fuerteventura (Canary Islands): International Journal of Earth Sciences, **94**, 301–316, doi: 10.1007/s00531-005-0471-6.
Nagihara, S., and S. A. Hall, 2001, Three-dimensional gravity inversion using simulated annealing: Constraints on the diapiric roots of allochthonous salt structures: Geophysics, **66**, 1438–1449, doi: 10.1190/1.1487089.
Oktay, O., J. Schlemper, L. L. Folgoc, M. Lee, M. Heinrich, K. Misawa, K. Mori, S. McDonagh, N. Y. Hammerla, and B. Kainz, 2018, Attention U-Net: Learning where to look for the pancreas: arXiv preprint, doi: 10.48550/arXiv.1804.03999.
Özbeyaz, A., and M. Söylemez, 2020, Modeling compaction parameters using support vector and decision treeregression algorithms: Turkish Journal of Electrical Engineering and Computer Sciences, **28**, 3079–3093, doi: 10.3906/elk-1905-179.
Paul, P., 2009, Predictors of work injury in underground mines — An application of a logistic regression model: Mining Science and Technology (China), **19**, 282–289, doi: 10.1016/S1674-5264(09)60053-3.
Press, F., 1968, Earth models obtained by Monte Carlo inversion: Journal of Geophysical Research, **73**, 5223–5234, doi: 10.1029/JB073i016p05223.
Press, F., 1970a, Regionalized earth models: Journal of Geophysical Research, **75**, 6575–6581, doi: 10.1029/JB075i032p06575.
Press, F., 1970b, Earth models consistent with geophysical data: Physics of the Earth and Planetary Interiors, **3**, 3–22, doi: 10.1016/0031-9201(70)90039-7.
Qin, P., D. Huang, Y. Yuan, M. Geng, and J. Liu, 2016, Integrated gravity and gravity gradient 3D inversion using the non-linear conjugate gradient: Journal of Applied Geophysics, **126**, 52–73, doi: 10.1016/j.jappgeo.2016.01.013.
Ronneberger, O., P. Fischer, and T. Brox, 2015, U-Net: Convolutional networks for biomedical image segmentation: 18th International Conference on Medical Image Computing and Computer-Assisted Intervention.
Ruppert, D., 1997, Empirical-bias bandwidths for local polynomial nonparametric regression and density estimation: Journal of the American Statistical Association, **92**, 1049–1062, doi: 10.1080/01621459.1997.10474061.
Sambridge, M., and K. Mosegaard, 2002, Monte Carlo methods in geophysical inverse problems: Reviews of Geophysics, **40**, 3-1–3-29, doi: 10.1029/2000RG000089.
Sampietro, D., M. Capponi, E. Thébault, and L. Gailler, 2023, An empirical method for the optimal setting of the potential fields inverse problem: Geophysical Prospecting, **71**, 350–365, doi: 10.1111/1365-2478.13305.
Sui, J., Y. Tian, Y. Li, and N. Wu, 2023, Complete perception self-attention network for weak seismic signal recovery in distributed acoustic sensing vertical seismic profile data: Geophysics, **88**, no. 6, WC107–WC119, doi: 10.1190/geo2022-0714.1.
Sun, H., Y. Feng, Y. Fu, W. Sun, C. Peng, X. Zhou, and D. Zhou, 2022, Bathymetric prediction using multisource gravity data derived from a parallel linked BP neural network: Journal of Geophysical Research: Solid Earth, **127**, e2022JB024428, doi: 10.1029/2022JB024428.
Tao, M., M. Jorgensen, and M. S. Zhdanov, 2021, Mapping the salt structures from magnetic and gravity gradiometry data in Nordkapp Basin, Barents Sea: First International Meeting for Applied Geoscience & Energy, SEG, Expanded Abstracts, 874–878, doi: 10.1190/segam2021-3583664.1.
Tarantola, A., 2005, Inverse problem theory and methods for model parameter estimation: SIAM.
Tarantola, A., and B. Valette, 1982, Generalized nonlinear inverse problems solved using the least squares criterion: Reviews of Geophysics, **20**, 219–232, doi: 10.1029/RG020i002p00219.
Tian, Y., X. Ke, and Y. Wang, 2019, A folding calculation method based on the preconditioned conjugate gradient inversion algorithm of gravity gradient tensor: Pure and Applied Geophysics, **176**, 215–234, doi: 10.1007/s00024-018-1965-z.
Tian, Y., J. Sui, Y. Li, N. Wu, and D. Shao, 2022, A novel iterative PA-MRNet: Multiple noise suppression and weak signals recovery for downhole DAS data: IEEE Transactions on Geoscience and Remote Sensing, **60**, 1–14, doi: 10.1109/TGRS.2022.3170635.
Tikhonov, A. N., and V. I. Arsenin, 1977, Solutions of ill-posed problems: Winston 14.
Tseng, C.-C., and S.-L. Lee, 2021, Implementation of temperature data denoising operator using steepest descent method: 20th International Symposium on Communications and Information Technologies.
Tu, X., and M. S. Zhdanov, 2022, Joint focusing inversion of marine controlled-source electromagnetic and full tensor gravity gradiometry data: Geophysics, **87**, no. 5, K35–K47, doi: 10.1190/geo2021-0691.1.
Wang, R., Y. Ding, Z. Xu, M. S. Zhdanov, M. Xian, Y. Zhang, J. Li, C. Jiang, and Z. Guo, 2024, Employing MS-UNets networks for multiscale 3D gravity data inversion: A case study in the Nordkapp Basin, Barents Sea: IEEE Transactions on Geoscience and Remote Sensing, **62**, 4502813, doi: 10.1109/TGRS.2024.3362070.
Wang, R., Z. Xu, C. Lai, X. Wang, M. S. Zhdanov, G. Li, Z. Cheng, J. Li, G. Zhao, and S. Liang, 2023, Reconstructing 2-D basement relief using gravity data by deep neuron network: An application on Poyang Basin: IEEE Transactions on Geoscience and Remote Sensing, **62**, 4500911, doi: 10.1109/TGRS.2023.3340523.
Wang, T.-H., D.-N. Huang, G.-Q. Ma, Z.-H. Meng, and Y. Li, 2017, Improved preconditioned conjugate gradient algorithm and application in 3D inversion of gravity-gradiometry data: Applied Geophysics, **14**, 301–313, doi: 10.1007/s11770-017-0625-x.
Wei, X., and J. Sun, 2021, Uncertainty analysis of 3D potential-field deterministic inversion using mixed Lp norms: Geophysics, **86**, no. 6, G133–G158, doi: 10.1190/geo2020-0672.1.
Wei, X., and J. Sun, 2022, 3D probabilistic geology differentiation based on airborne geophysics, mixed Lp norm joint inversion, and physical

Downloaded from http://pubs.geoscienceworld.org/seg/geophysics/article-pdf/89/5/G93/6947062/geo-2023-0551.1.pdf
by Univ Utah Marriott Library user

property measurements: Geophysics, **87**, no. 4, K19–K33, doi: 10.1190/geo2021-0833.1.
Wei, X., J. Sun, and M. K. Sen, 2023, Quantifying uncertainty of salt body shapes recovered from gravity data using trans-dimensional Markov chain Monte Carlo sampling: Geophysical Journal International, **232**, 1957–1978, doi: 10.1093/gji/ggac430.
Wu, X., J. Ma, X. Si, Z. Bi, J. Yang, H. Gao, D. Xie, Z. Guo, and J. Zhang, 2023, Sensing prior constraints in deep neural networks for solving exploration geophysical problems: Proceedings of the National Academy of Sciences, **120**, e2219573120, doi: 10.1073/pnas.2219573120.
Xu, Z., L. Wan, and M. S. Zhdanov, 2020, Focusing iterative migration of gravity gradiometry data acquired in Nordkapp Basin, Barents Sea: Geophysical Prospecting, **68**, 2292–2306, doi: 10.1111/1365-2478.12990.
Xu, Z., R. Wang, W. Xiong, J. Wang, and D. Wang, 2021a, 3D hybrid imaging based on gravity migration and regularized focusing inversion to predict the Poyang Basin interface: Geophysics, **86**, no. 4, G55–G67, doi: 10.1190/geo2020-0396.1.
Xu, Z., G. Zou, Q. Wei, J. Tian, and H. Yuan, 2021b, Focusing joint inversion of gravity and magnetic data using a clustering stabilizer in a space of weighted parameters: Geophysical Journal International, **224**, 1344–1359, doi: 10.1093/gji/ggaa518.
Zhang, J., and G. Sheng, 2020, First arrival picking of microseismic signals based on nested U-Net and Wasserstein generative adversarial network: Journal of Petroleum Science and Engineering, **195**, 107527, doi: 10.1016/j.petrol.2020.107527.
Zhang, R., T. Li, C. Liu, X. Huang, K. Jensen, and M. Sommer, 2021, 3-D joint inversion of gravity and magnetic data using data-space and truncated Gauss-Newton methods: IEEE Geoscience and Remote Sensing Letters, **19**, 1–5, doi: 10.1109/LGRS.2021.3077936.
Zhao, S., D. Liu, Q. Yuan, and J. Li, 2020, A global gravity reconstruction method for mercury employing deep convolutional neural network: Remote Sensing, **12**, 2293, doi: 10.3390/rs12142293.
Zhdanov, M. S., 2015, Inverse theory and applications in geophysics: Elsevier 36.
Zhdanov, M. S., and W. Lin, 2017, Adaptive multinary inversion of gravity and gravity gradiometry data: Geophysics, **82**, no. 6, Q101–Q114, doi: 10.1190/geo2016-0451.1.
Zhou, Z., M. M. Rahman Siddiquee, N. Tajbakhsh, and J. Liang, 2018, U-Net++: A nested U-Net architecture for medical image segmentation: Deep learning in medical image analysis and multimodal learning for clinical decision support: 4th International Workshop, DLMIA 2018, and 8th International Workshop, ML-CDS 2018.

Biographies and photographs of the authors are not available.

Downloaded from http://pubs.geoscienceworld.org/seg/geophysics/article-pdf/89/5/G93/6947062/geo-2023-0551.1.pdf
by Univ Utah Marriott Library user